Chemosphere 281 (2021) 130837

Contents lists available at ScienceDirect

Chemosphere

journal homepage: www.elsevier.com/locate/chemosphere

Montmorillonite-iron crosslinked alginate beads for aqueous phosphate removal

Tonoy K. Das, Quentin Scott, Achintya N. Bezbaruah *

Nanoenvirology Research Group, Department of Civil and Environmental Engineering North Dakota State University, Fargo, ND, 58105, USA

ARTICLE INFO

Handling Editor: Y Yeomin Yoon

Keywords:
Montmorillonite clay
Alginate
Iron crosslink
Phosphate
Eutrophic lakes

ABSTRACT

Phosphate runoff from agriculture fields leads to eutrophication of the water bodies with devastating effects on the aquatic ecosystem. In this study, naturally occurring montmorillonite clay-incorporated iron crosslinked alginate biopolymer (MtIA) beads were synthesized and evaluated for aqueous phosphate removal. Batch experiment data showed an efficient phosphate removal (>99%) by the MtIA beads from solutions with different initial phosphate concentrations (1 and 5 mg PO_4^{3-}-P/L, and 100 μg PO_4^{3-}-P/L). The kinetic data fitted well into the pseudo-second-order kinetic model indicating chemisorption played an important role in phosphate removal. Based on analyses of results from the Elovich and intra-particulate diffusion models, phosphate removal by the MtIA beads was found to be chemisorption where both film diffusion and intra-particulate diffusion participated. The isotherm studies indicate that MtIA surfaces were heterogeneous, and the adsorption capacity of the beads calculated from Langmuir model was 48.7 mg PO_4^{3-}-P/g of dry beads which is ~2.3 times higher than values reported for other clay-metal-alginate beads. Electron microscopy (SEM-EDS) data from the beads showed a rough-textured surface which helped the beads achieve better contact with the phosphate ions. Fourier-transform infrared spectroscopy (FTIR) indicated that both iron and montmorillonite clay participated in crosslinking with the alginate chain. The MtIA beads worked effectively (>98% phosphate removal) over a wide pH range of 2–10 making it a robust adsorbent. The beads can potentially be used for phosphate recovery from eutrophic lakes, agricultural run-off, and municipal wastewater.

1. Introduction

Phosphorus (P) is one of the major growth-limiting macronutrients for plants, specifically for crops. The global consumption of phosphatic fertilizer is increasing due to high-input modern agricultural practices. In the last two decades, phosphatic fertilizer use increased from ~32.3 million tons (2000) to 45.1 million tons (2017) (FAO, 2020), and it is expected to increase further as we try to meet the food demand for the rapidly growing global population. The phosphorus use efficiency in our agricultural system is very low (15–20%) (Patle et al., 2019). While most of the applied phosphorus gets immobilized onto the topsoil layer, and become non-bioavailable to plants, and a major part ends up in different waterbodies through surface and subsurface runoff as well as because of soil erosion (Kleinman et al., 2015). The excess phosphorus in waterbodies causes eutrophication that triggers aquatic plant bloom and the associated depletion of dissolved oxygen, and that severely affects the water quality, disrupting the aquatic ecosystem (Glibert, 2020; Meinikmann et al., 2015).

In the United States, many waterbodies are impacted by high phosphorus concentration (with >30 μg PO_4^{3-}-P/L being eutrophic), and they include lakes (>42% of all lakes in the US) and rivers/streams (>66%) (USEPA, 2009). Besides adversely affecting environmental quality and aquatic ecosystem, eutrophication also affects the economy by increasing the treatment needs for drinking water (Duan et al., 2017), impacting fishery activities (Ruuhijarvi et al., 2010), and reducing the recreational value of the waterbodies (Dodds et al., 2009). Phosphorous in waterbodies are mostly orthophosphates present in very low concentrations (Boyd, 2019) yet causes eutrophication (>30 μg PO_4^{3-}-P/L). There is a need to develop technologies for the effective removal of aqueous phosphate specifically when present in low concentrations.

Phosphorus is also a non-renewable mined resource. The supply of good quality mineable rock phosphate (mineral P) is predicted to last for only 60–240 years if the current consumption rate continues, and it is predicted that phosphate supply will potentially fall short of demand by the year 2033 (Ober, 2016). So, there is an urgent need to find alternate sources of phosphorus. Phosphorus in the impaired (eutrophic)

* Corresponding author.
E-mail address: a.bezbaruah@ndsu.edu (A.N. Bezbaruah).

https://doi.org/10.1016/j.chemosphere.2021.130837
Received 13 March 2021; Received in revised form 4 May 2021; Accepted 5 May 2021
Available online 11 May 2021
0045-6535/© 2021 Elsevier Ltd. All rights reserved.

waterbodies can be one of the future sources of phosphorus, and its use in agriculture would enhance sustainability by creating a cyclic process.

There are numerous technologies available for aqueous phosphate removals which include biological methods, electrocoagulation, ion-exchange, membrane processes, and adsorption. However, removal of phosphate from eutrophic lakes is very challenging given, among other things, the ultra-low concentration of phosphate ($\leq$100 μg PO_4^{3-}-P/L). Typical phosphate concentrations reported in eutrophic lakes range from 30 to 100 μg PO_4^{3-}-P/L (Robertson et al., 2003; Wetzel, 2001). Phosphorus enters the surface waterbodies as either dissolve phosphate or phosphorus loaded onto sediments and organics (Carpenter, 2005). Phosphorous strongly binds with the sediments if Fe_2O_3, CaO, and organic matters are present in sediments (Randall et al., 2019), but phosphorus trapped in the legacy sediments is released to the bulk water via physico-chemical and biological processes (Li et al., 2019). Reduction of internal P-loading from sediments has been tried by sediment dredging (Jing et al., 2015) but that is very expensive. The disposal and/or storage of dredged sediments, potential release of other toxic substances, increase in phytoplankton productivity, and temporary reduction in benthic fish food (organisms) are other major issues associated with dredging (Bormans et al., 2016). The addition of chemical flocculants (Al-, Fe-, or Ca-based chemicals) has been proposed (Lin et al., 2015) but that involves the introduction of foreign chemicals to the waterbodies and leads to the deposition of P-rich sediments. In-situ sediment capping has also been proposed as a potential option for remediating eutrophic waters (Wang and Jiang, 2016), but this is cost-prohibitive. Biological processes like enhanced biological phosphorus removal are well established but very much limited to the treatment of municipal wastewater which has high phosphate concentration (5–10 mg P/L) (Yang et al., 2017), and it is not feasible for use in eutrophic lakes with very low aqueous phosphate (Ritt et al., 2019). Membrane processes like ultra-filtration and nanofiltration can effectively remove phosphate from aqueous phase. Ion-exchange technology can also be very effective. However, they are suitable for relatively small volume of water and not useable for large surface waterbodies (Ritt et al., 2019). The complexity involved in the management of the phosphorus cycle in eutrophic waterbodies like lakes make it very difficult to get rid phosphorus totally, but we can strategize to recover the phosphate for use in agriculture (Ritt et al., 2019).

Adsorption is considered by many as one of the best options for phosphate removal from waters (Bacelo et al., 2020; Ramasahayam et al., 2014). Adsorption technology has potential for large-scale application due to its ease of implementation and economic feasibility (Kumar et al., 2019a). An ideal adsorbent should be cost-effective, environmentally benign, selective for phosphate with high adsorption capacity, and have quick reaction kinetics. The phosphate adsorbed onto such an adsorbent should be reusable for other purposes like agriculture.

Clay minerals have a natural affinity for phosphate (Gérard, 2016). Among the clay minerals, naturally occurring montmorillonite has a relatively high specific surface area (BET specific surface area of ~33 m^2/g) and surface charge (cation exchange capacity of ~85 meq/100 g of clay) (Le Forestier et al., 2010). The montmorillonite clay is a 2:1 type aluminosilicate mineral where one alumina octahedral sheet is sandwiched between two silica tetrahedral sheets and fused together to form a one-unit cell structure (Fig. S1). The surface of the montmorillonite is highly negatively charged which comes from the isomorphous substitution of lower valance cations in the tetrahedral (Si^{4+} substituted by Al^{3+}) and the octahedral (Al^{3+} substituted by Mg^{2+}).

In this study, we used a montmorillonite clay mineral in iron crosslinked alginate biopolymer beads to remove aqueous phosphate. Further, iron used for alginate crosslinking was expected to crosslink with montmorillonite given its negatively changed surfaces. We used Fe^{3+} as the cross-linker instead of conventional Ca^{2+} (in Ca-alginate beads) as iron and iron oxides have been used as efficient phosphate adsorbents (Almeelbi and Bezbaruah, 2012; Hossain et al., 2018; Liu et al., 2018). Phosphate sorption by MtIA beads was evaluated based on the data from adsorption and batch kinetics studies. The role of the clay mineral in phosphate removal was investigated and possible mechanisms have been proposed.

2. Experimental section

2.1. Chemicals and reagents

Iron (III) chloride tetrahydrate ($FeCl_3{\cdot}4H_2O$, reagent grade, Alfa Aesar, USA), monopotassium phosphate (KH_2PO_4, 99% pure, EMD Chemicals, Germany), sodium alginate $(C_6H_7NaO_6)_n$, production-grade, Spectrum Chemical, USA), sodium hydroxide (NaOH, ACS Grade, BDH, USA), and Na-rich montmorillonite (SWy-2 clay, The Clay Minerals Society, USA) were used as received unless otherwise specified. Laboratory produced deionized (DI, 17.8 MΩ-cm) water was used in this study.

2.2. Synthesis of montmorillonite clay iron crosslink beads (MtIA)

Sodium alginate (2 g) was dissolved in 50 mL of deionized (DI) water by continuous stirring and heating (~40 °C) for 1 h and then the solution was continuously stirred overnight at room temperature (22 ± 2 °C) to form an alginate gel. Separately, 5 g of montmorillonite clay (Mt) was suspended in 50 mL of DI water and stirred continuously until it formed a smooth slurry. The smooth clay slurry was then mixed with the alginate gel and stirred continuously (at room temperature) to make a homogeneous Mt-alginate solution (2% alginate and 5% clay). The Mt-alginate solution was released dropwise into a ferric chloride solution (2% w/v) at room temperature using a micropipette tip fitted to a silicone tube (L/S 16, Masterflex Precision Pump Tubing) connected to a peristaltic pump (Masterflex, Cole-Palmer, USA) (Fig. 1a). Mt-iron crosslinked alginate beads (MtIA) were formed as soon as the Mt-alginate solution came in contact with the iron solution. The freshly formed beads were kept submerged in 2% $FeCl_3$ solution overnight (24 h) in a 500 mL beaker for the beads to harden (Bezbaruah et al., 2009; Hossain et al., 2018). The hardened beads were washed with a copious amount of DI water to remove the excess $FeCl_3$ and the washed beads were stored in DI water for later use. For phosphate removal studies, the beads were taken out of the water and the excess water was blotted with tissue papers. The weight of the beads is reported either as wet weight or as dry weight (dried at 60 °C for 12 h). For control experiments, beads were produced using the same procedure but without the Mt-clay.

2.3. Material characterization

The surface morphology of the synthesized beads was examined using scanning electron microscopy (SEM, JEOL JSM-7600F, JEOL USA, Peabody, MA). The elemental composition of the beads was determined with energy-dispersive spectroscopy (EDS) using UltraDry silicon drift X-ray detector and NSS-212e NORAN System 7 X-ray microanalysis system (ThermoFisher Scientific, Madison, WI) which was attached to the SEM. The beads were observed before and after reaction with phosphate. The samples for SEM-EDS analysis were prepared by drying the beads under a vacuum condition in a nitrogen environment. Dried beads (some intact and some cut in half with a razor blade to reveal the internal structure) were attached to aluminum mounts with carbon tapes.

Fourier transform infrared (FTIR) spectra of fresh (before phosphate adsorption) and spent (after phosphate adsorption) MtIA beads were recorded using a Nicolet 8700 FTIR spectrometer and analyzed using OMNIC software (ThermoFisher Scientific, Waltham, MA). For FTIR analyses, the beads were first dried in a vacuum oven in a nitrogen environment for 24 h, the dried beads were then crushed into a fine powder. The powdered sample was mixed with potassium bromide (KBr) which acted as the IR transparent background. The spectra were measured in the range of 4000–400 cm^{-1} with a resolution of 4 cm^{-1}

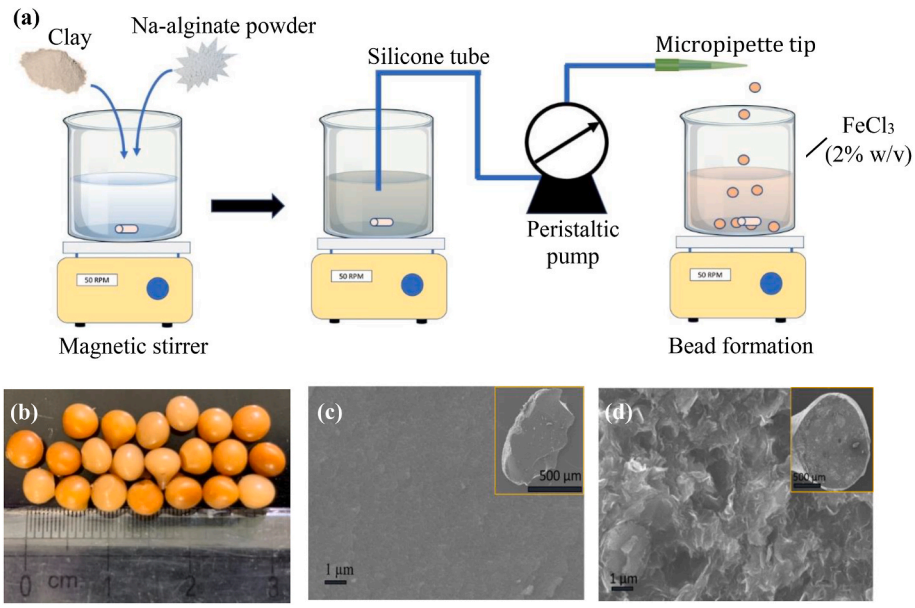

Fig. 1. (a) Schematic of montmorillonite iron cross-linked alginate (MtIA) bead synthesis process. (b) Photograph of freshly produced MtIA beads; (c) SEM micrograph of a control bead; and (d) SEM micrograph of a MtIA bead with each inset showing a cross-section of the bead. The surface of the control bead was smooth, and the bead shrunk to become oblong upon drying. The MtIA bead surface showed rough texture due to the presence of the clay mineral, the bead maintained its spherical shape upon drying.

and each spectrum was composed of 32 scans.

2.4. Phosphate batch, kinetic and isotherm studies

For all the phosphate removal experiments 5 g of wet beads (0.48 ± 0.02 g dry weight) and 45 mL of phosphate solution were placed in 50 mL polypropylene plastic vials (reactors) fitted with a plastic cap. The reactors were rotated in a custom-made end-over-end shaker (28 rpm) at room temperature to reduce mass transfer resistance. The phosphate removal performance of the MtIA beads was determined in batch experiments (24 h) with an initial phosphate concentration of 10 mg PO_4^{3-}-P/L. Controls with control beads (no clay) and blanks (with no beads) were run simultaneously. The kinetics of phosphate removal by MtIA beads were studied with three PO_4^{3-}-P concentrations (1 and 5 mg/L, and 100 µg/L). The 100 µg/L PO_4^{3-}-P was selected as that is an environmentally relevant concentration representing eutrophic lakes. A set of reactors was rotated in the end-over-end shaker up to 12 h. At least three reactors were taken out at specific time intervals (0, 5, 10, 15, 30, 60, 180, 360, and 720 min) and the bulk solution was separated from the reactors by decanting it. The bulk solution from each reactor was stored separately in the refrigerator for further analysis. The phosphate concentrations in the bulk solution were measured in a Hach DR 5000 spectrophotometer (880 nm, detection limit 10 µg PO_4^{3-}-P/L) using the ascorbic acid method (Eaton et al., 2005). The phosphate removal efficiency (η) was calculated as $\eta = (C_0 - C_e)/C_0$ x100%, where C_0 and C_e are the initial and equilibrium phosphate concentrations. The bulk solution phosphate concentration data (average of three values at each time point) were used for reaction order determination. Zero- (Eq. (1)), first- (Eq. (2)), second- (Eq. (3)), pseudo-first- (Eq. (4)) (Ho and McKay, 1998), and pseudo-second- (Eq. (5)) (Ho and McKay, 1998) order models were used for data analysis.

$$C_t = C_0 - kt \tag{1}$$

$$\ln(C_t) = \ln(C_0) - kt \tag{2}$$

$$\frac{1}{Ct} = kt + \frac{1}{C_0} \tag{3}$$

$$\log(q_e - q_t) = \log q_e - \frac{k_1 t}{2.303} \tag{4}$$

$$\frac{t}{q_t} = \frac{1}{k_2 q_e^2} + \frac{t}{q_e} \tag{5}$$

For Eqs. (1)–(5), C_t is the concentration at time t, C_0 is the initial concentration, q_e (mg/g) is the equilibrium adsorption capacity of the adsorbent (beads), q_t (mg/g) is adsorption capacity at time t, k_1 (1/min) is the rate constant for the pseudo-first-order reaction, and k_2 (g/mg/min) is the rate constant for the pseudo-second-order reaction. The log (q_e-q_t) vs t plot gives the value of k_1 and q_e for the pseudo-first-order reaction, and t vs t/q_t plot helps in q_e, and k_2 determination (pseudo-second-order reaction).

Phosphate adsorption isotherm experiment was carried out with MtIA beads in batch reactors (5 g of wet ≈ 0.48 g dry beads in 45 mL solution in 50 mL reactors) with initial phosphate concentration varied from 10 to 2515 mg PO_4^{3-}-P/L. The reactors were rotated in the end-over-shaker for 24 h and the bulk solution phosphate concentration was measured. The phosphate sorption capacity was calculated as $q_e = (C_0 - C_e)$ x V/m where q_e is the mass of phosphate per gram of dry MtIA bead (mg PO_4^{3-}-P/g of dry bead), V is the volume of phosphate solution (L), and m is dry mass of MtIA beads (g). The adsorption isotherm data were fitted onto Langmuir (Eq. (6)) and Freundlich (Eq. (7)) isotherm models to get insight into the adsorption mechanism.

$$q_e = \frac{q_{max}\, C_e\, K_l}{1 + K_l C_e} \tag{6}$$

$$q_e = k_f C_e^{\,1/n} \tag{7}$$

In Eqs. (6) and (7), q_{max} (mg/g) is the maximum adsorption capacity, k_l (L/mg) is the Langmuir constant (which represents the affinity between the solute and adsorbent), k_f is the Freundlich constant, and 1/n is the adsorption intensity ($1 < n < 10$). The Langmuir model represents monolayer adsorption whereas the Freundlich model fits well for an adsorbent with significant surface heterogeneity.

2.5. Quality control

All experiments were performed at room temperature and in triplicate, and the average values are reported here along with the standard deviations. ANOVA analyses were performed using OriginLab (Version, 2020) to evaluate the significant differences between the data sets and Tukey's pairwise comparison was used to identify the data that were significantly different.

3. Results and discussion

3.1. Characterization

3.1.1. Morphology and composition

The surface morphologies of control and MtIA beads (Fig. 1c and d) were observed based on SEM micrographs of the beads. Alginate beads without Mt-clay (control) were also examined for comparison. While the controls (beads with no Mt-clay) had a smoother surface (Fig. 1c), the MtIA bead surface (Fig. 1d) appeared as a rough-textured surface due to the presence of clay particles. The surface roughness might have increased the contact surface area of the beads and helped in the absorption of water and the solute (Fernandes et al., 2017). Na-rich montmorillonite (SWy-2) clay has a size distribution of 5–750 nm with an average size of 250 nm (Michot et al., 2004)). Montmorillonite clay minerals have surface hydroxyl groups that interact with phosphate ions. Further, clay mineral surfaces act as support sites for iron oxide/hydroxide formation in the MtIA beads. The MtIA bead surface did not shrink when they were vacuum dried and remained spherical (Fig. 1d inset) but the controls shrunk to an oblong shape (Fig. 1c inset). The EDS analysis of fresh control beads (Fig. 2a) shows carbon (C), oxygen (O), iron (Fe), and chloride (Cl). The presence of a high amount of iron (~48.9%) indicates that the iron was successfully incorporated within the alginate polymeric network. During control bead formation sodium ion (Na^{+}) was replaced by iron (Fe^{3+}) through ionic crosslinking to the alginate network structure (Fig. 3a). This is supported by our EDS result where sodium is not detected. Further, no sodium (Na) was observed in the MtIA beads (Fig. 2b) even though Na^{+} ion was originally present in the interlayer of Mt clay connecting two-unit cell (one Al octahedral sandwich between two Si tetrahedral, Fig. 3b); this might have possibly happened because the Na^{+} ions were displaced during the crosslinking process. In presence of water, the interlayer of Mt-clay expanded, and the iron-alginate polymer units got access to the interlayer, and the polymer units expelled out the Na^{+} ions from the clay minerals (Fig. 3b) (Fernandes et al., 2018). The presence of high Fe and no detectable Na in MtIA beads confirms this. The MtIA beads showed additional elements including magnesium (Mg), silicon (Si), aluminum (Al), and potassium (K), and they came from the montmorillonite clay. There was a significant reduction in the weight percent of Fe in the MtIA beads (~11.7%) compared to the control beads (~48.9%). This indicates that Mt-clay particles also took part in the crosslinking process (Fernandes et al., 2018; Ravi and Pandey, 2019) unlike in the control beads where Fe was the main crosslinking agent.

3.1.2. Fourier transform infrared spectroscopy (FTIR)

The FTIR data were collected to gain insight into the molecular interactions of freshly prepared MtIA beads (Fig. 2c) and the data were compared to that obtained from the control unit. The broad band

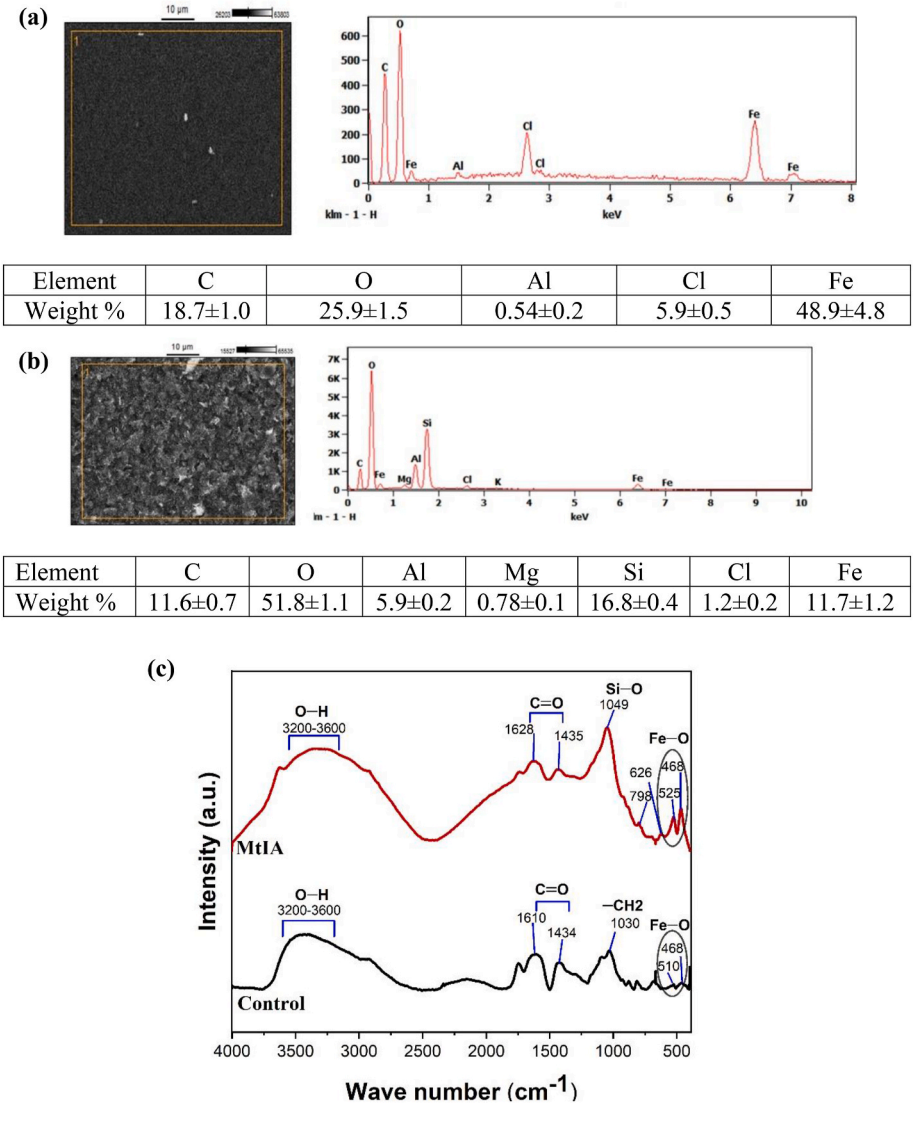

Element	C	O	Al	Cl	Fe
Weight %	18.7±1.0	25.9±1.5	0.54±0.2	5.9±0.5	48.9±4.8

Element	C	O	Al	Mg	Si	Cl	Fe
Weight %	11.6±0.7	51.8±1.1	5.9±0.2	0.78±0.1	16.8±0.4	1.2±0.2	11.7±1.2

Fig. 2. SEM-EDS of (a) control bead; (b) MtIA bead. There was a significant decrease in iron content in the MtIA beads (~11.7%) compared to the control beads (~48.9%). In the MtIA beads, noticeable amounts of Si and Al were recorded which came from Mt-clay (aluminosilicate); and (c) FTIR spectra for the control and MtIA beads. The broadband of 3200–3600 cm^{-1} in both spectra came from –OH stretching of alginate polymer. The carboxylate asymmetric stretching vibration shifted in MtIA (1628 cm^{-1}) and control (1610 cm^{-1}) confirming the introduction of the clay mineral in the alginate network. Further, characteristic peak Fe–O vibration appeared in each polymer bead confirming Fe-ion crosslinking with alginate.

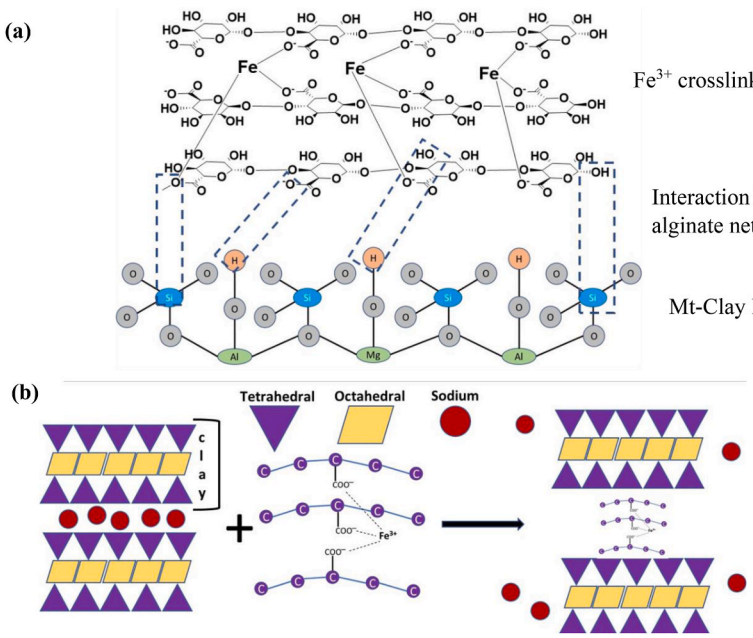

Fig. 3. (a) Possible crosslinking process of Fe^{3+} to the alginate network and interaction with clay mineral surface. Crosslinked alginate chain and silicate clay layer are connected at several points through electrostatic and intermolecular hydrogen bonds which create a three-dimensional network; and (b) Possible clay polymer network configuration. The iron crosslinked alginate accesses the interlayer between two montmorillonite units and expels the interlayer Na^{+} (Figures modified after Fernandes et al., 2018).

identified between 3200 and 3600 cm^{-1} in both beads corresponds to –OH stretching which came from the alginate polymer chains (Papageorgiou et al., 2010). Characteristic bands due to asymmetric and symmetric stretching vibration of the carboxyl group of an alginate molecule appeared at 1610 and 1434 cm^{-1} (Papageorgiou et al., 2010; Zhang et al., 2020) for the controls and 1628 and 1435 cm^{-1} for MtIA. The asymmetric stretching vibration of a carboxylate shifted to higher wavenumbers in MtIA beads (1628 cm^{-1}) compared to the control beads (1610 cm^{-1}) due to the introduction of Mt-clay minerals. A group of distinguishable bands appeared in MtIA beads at 1049, 798, 626 cm^{-1} and could be attributed to Si–O stretching in the Si-tetrahedral of Mt-clay minerals (Barreca et al., 2014; Fabryanty et al., 2017), and confirmed the presence of Mt-clay in the beads. In the control beads, $–CH_2$ bending appeared at 1030 cm^{-1} and overlapped with Si–O stretching at 1049 cm^{-1} in the MtIA beads. The band at 1049 cm^{-1} from the MtIA beads is related to Si–O–Si axial deformation into and out of the plane of the tetrahedral site (Fernandes et al., 2018). The Fe–O vibration bands were identified at 510 and 468 cm^{-1} in the control beads, and 525 and 468 cm^{-1} in the MtIA beads, and that confirmed the successful crosslinking of alginate by iron (Namduri and Nasrazadani, 2008).

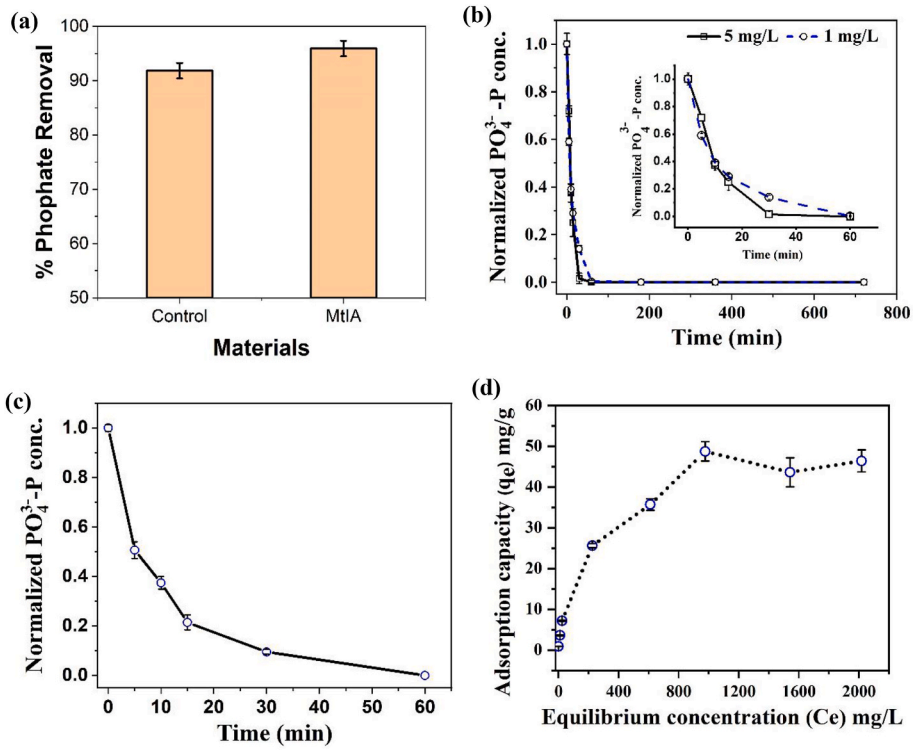

Fig. 4. (a) Phosphate removal by MtIA beads (C_0 = 10 mg PO_4^{3-}-P/L, Adsorbent dose = 5 g wet beads in 45 mL solution); and (b) Phosphate removal by MtIA beads over time from solutions with two different initial PO_4^{3-}-P concentrations (5 and 1 mg/L). Inset: the first 60 min zoomed in; (c) Phosphate removal by MtIA with initial PO_4^{3-}-P concentration of 100 μg/L; and (d) Adsorption isotherm for phosphate sorption onto MtIA. The data points are connected with straight lines for ease of reading only and they do not represent trendlines. The vertical error bars represent ± standard deviations.

3.2. Batch studies for phosphate removal and effects of pH

The phosphate removal performances of the MtIA bead were compared (Fig. 4a) using aqueous phosphate with an initial concentration (C_0) of 10 mg PO_4^{3-}-P/L. The MtIA beads recorded ~96% phosphate removal. The phosphate removal by alginate beads without Mt-clay (control) was also evaluated for comparison. The MtIA beads removed 4% more phosphorus (statistically significant at $p = 0.05$) than the controls (~92% phosphate removal). The higher removal by MtIA beads was observed potentially because of better contact between the bead and the phosphate solution due to its surface roughness (both external and internal surfaces). Further, phosphate was also adsorbed onto Mt clay minerals. The effects of pH on phosphate removal ($C_0 = 5$ mg PO_4^{3-}-P/L) by the MtIA beads were monitored for a wide pH range (pH 2–10) in a DI water system adjusting the initial solution pH using 0.1 M NaOH or HCL (Fig. S2a). The phosphate removal remained at ~98–99% for all pH values. The point-of-zero-charge (PZC) for the MtIA beads was found to be 3.14 (Fig. S2b) indicating that the surface of the beads is positively charged when solution pH is below PZC and negatively charged at pH > 3.14 (above PZC). At a pH lower than the PZC, the negatively charged phosphate ions electrostatically get attached to the bead surface. With increasing pH (pH > 3.14), the negatively charged bead surface repulses phosphate ions and that should lead to a reduction in phosphate removal. However, pH was found to have minimal effect on phosphate removal by the beads (Fig. S2a) indicating that the removal process is not exclusively controlled by electrostatic interaction but surface complexation may be involved. The versatility of the MtIA beads over a wide pH range makes the beads very robust and it will work effectively in eutrophic lakes where the typical pH is 7.5–8.5 (Ritt et al., 2019).

3.3. Removal kinetics

Phosphate removal by MtIA bead was evaluated at environmentally relevant high ($C_0 = 1$ and 5 mg PO_4^{3-}-P/L) and low ($C_0 = 100$ μg PO_4^{3-}-P/L) initial concentrations (Fig. 4b and c) over a 720 min (12 h) period. While 1–5 mg/L is the typical phosphate concentration in municipal wastewater, 100 μg/L PO_4^{3-}-P is representative of eutrophic lakes (PO_4^{3-}-P > 30 μg/L causes eutrophication). For all phosphate concentrations, MtIA beads reached equilibrium within 30 min with the phosphate concentration reduced below the instrument detection limit (~100% removal). The removal kinetics followed similar patterns for all the three concentrations with rapid removal in the first 10 min (~62%) followed by a relatively slow removal till an equilibrium is reached at 30 min.

To investigate the mechanism of phosphate removal by the MtIA beads and determine the rate-controlling factors, the batch study data (first 60 min) were fitted into five different models (zero-, first-, second-, pseudo-first-, and pseudo-second-order models) (Fig. S3-4). The data fitted the best into pseudo-second-order kinetic model for all three PO_4^{3-}-P concentrations used (5 mg/L: $R^2 = 0.9714$, 1 mg/L: $R^2 = 0.9996$, and 100 μg/L: $R^2 = 0.9992$) (Table 1, Fig. S4). Given that the data fitted into the pseudo-second-order model, we can infer that chemisorption played an important role in the phosphate removal process, and the rate of adsorption was proportional to the square of the number of the unoccupied sites on the adsorbent surface and the concentration of adsorbate in the solution. The reaction rate constant for the pseudo-second-order model increased from 0.143 ($C_0 = 5$ mg PO_4^{3-}-P/L) to 14.958 mg/g/min ($C_0 = 100$ μg PO_4^{3-}-P/L) with decreasing solution phosphate concentration (Table 1), possibly because of the abundance of adsorption sites relative phosphate ions present.

Based on the batch study data, it can be inferred that a greater number of adsorption site were potentially available for phosphate adsorption at the beginning leading to a steep concentration gradient between the bead and phosphate in the bulk solution. However, the concentration gradient was decreased over time, and a slower reaction was observed. The adsorption of phosphate onto MtIA bead might have depended on diffusion of phosphate from bulk solution to the bead's external surface (external mass transfer) or adsorption onto external surface and subsequent diffusion into the internal pore (intraparticle diffusion). Kinetic data were fitted into the intraparticle diffusion model (Eq. (8), after Webber and Morris, 1963 (Weber and Morris, 1963)) to investigate whether diffusion played any significant role in the adsorption process.

$$q_t = k_p t^{0.5} + C \tag{8}$$

In Eq. (8), q_t (mg/g) is the phosphate sorption capacity of MtIA at time t (min), k_p is the intra-particle diffusion rate constant (mg/g-$min^{1/2}$) and C is the constant dependent on the thickness of the boundary layer. C is an indicator of the boundary layer effect (the higher the value of C, the greater the boundary layer effect). When q_t vs $t^{0.5}$ is plotted, k_p can be determined from the slope and C from the Y-intercept (Fig. S5). If the q_t vs $t^{0.5}$ plot is a straight line and passes through the origin, then intraparticle diffusion would be the only rate-limiting factor. In this study, the q_t vs $t^{0.5}$ plot (Fig S5) showed bi-linearity (i.e., two steps) indicating that intraparticle diffusion was not the only rate-limiting factor, but another mechanism (possibly, surface adsorption) was also involved in phosphate removal. The presence of the multi-linearity of the plot (Step 1 (S_1) and Step 2 (S_2)) is indicative of the presence of boundary layer diffusion and intraparticle diffusion followed by saturation step. The intra-particle diffusion rate constant (k_p) was higher in S_1 step compared to S_2 step for all three-phosphate concentrations tested (Table 1) indicating that adsorption initially took place on an external surface with a rapid adsorption rate. When all the external adsorption sites are occupied, phosphate ions started to diffuse into the internal pores of the bead. The rate constant (k_p) decreased in S_2 due to increased diffusion resistance in the internal pore surface and a decrease in phosphate concentration over time (Valderrama et al., 2008).

Table 1
Kinetic parameters associated with phosphate adsorption by the MtIA beads.

Kinetics Model	Parameter	Phosphate Concentration					
		5 mg/L		1 mg/L		100 μg/L	
Pseudo-second Order	R^2	0.9714		0.9996		0.9992	
	q_e	0.610		0.106		0.010	
	k_2	0.143		1.043		14.958	
Intra-particle Diffusion	R^2	0.7815		0.9297		0.9000	
		S_1	S_2	S_1	S_2	S_1	S_2
	R_i^2	0.9653	0.712	0.9870	0.9843	0.9833	0.9737
	k_p	0.1444	0.0302	0.0172	0.0068	0.0016	0.0005
	C	−0.1718	0.2809	0.0005	0.0409	0.0008	0.0054
Elovich-Mass Transfer	R^2	0.9100		0.9926		0.9733	
	α	0.1036		0.0278		526.315	
	β	6.8634		45.8715		4.1842×10^{-3}	

Units: q_e: mg/g; K_2: mg/g/min; k_p: mg/g $min^{1/2}$; C: mg/g; α: mg/g/min; β: g/mg. Notes: R^2: Overall correlation coefficient; R_i^2: Correlation coefficient for each step in the intra-particle diffusion model; S_1: Step 1 and S_2: Step 2 in the intra-particle diffusion model.

From the pseudo-second-order model (Eq. (5)), it is confirmed that chemisorption was the dominant mechanism of phosphate adsorption by MtIA, and so the Elovich model (Eq. (9)) was used to elucidate the chemisorption process in term of variation of chemisorption energetics with the extent of surface coverage (Teng and Hsieh, 1999). This model can also indicate whether the active sites are heterogeneous and therefore, exhibit different activation energies for chemisorption.

$$q_t = \frac{1}{\beta}\ln(\alpha\beta) + \frac{1}{\beta}\ln(t) \quad (9)$$

In Eq. (9), q_t (mg/g) is the phosphate sorption capacity at time t (min) and α is the initial sorption rate (mg/g-min) and β is the desorption constant (g/mg). In the plot of q_t vs ln(t), 1/β is given by the slope and 1/β ln(α β) is the Y-intercept. The correlation coefficients (R^2) for the Elovich model (Fig. S4) fitted with the experimental data for the three phosphate concentrations varied from 0.9100 to 0.9926 (Table 1) indicating that the adsorption of phosphate was controlled by chemisorption onto heterogonous adsorption sites in the MtIA beads.

3.4. Adsorption isotherms

The experimental adsorption data (Fig. 4d) were fitted into Langmuir, Freundlich, Temkin and Sips isotherm models (Table S1) to find out the type and nature of interactions of phosphate with MtIA beads, adsorption mechanisms, and the maximum phosphate adsorption capacity. Freundlich (R^2 = 0.9846) and Langmuir (R^2 = 0.9892) model fitted better than other isotherm models (Fig. S6). The very good fit (R^2 > 0.98) for both the models can be explained by the surface properties of the adsorbent and the affinity of the adsorbent for phosphate. That our data fitted the Freundlich model well points towards surface heterogeneity of the beads as well as the exponential distribution of the active sites and differences/variation in active site energies. The constant k_f is related to sorption capacity and 1/n is an empirical parameter related to the intensity of adsorption and adsorbate site heterogeneity. For 0 < 1/n < 1, the adsorption is favorable, and when 1/n is > 1, the adsorption process is unfavorable, and it is irreversible when 1/n = 1. The 1/n value obtained from the model is 0.4703 (0 < 1/n < 1) which means sorption of phosphate onto MtIA bead is favorable and the surface of MtIA is heterogeneous.

The adsorption isotherm data also fitted into the Langmuir model (R^2 = 0.9892). This indicates that monolayer adsorption occurred on the adsorption sites of the heterogeneous beads surface which consisted of several patches of smaller homogeneous surfaces, and this observation is in conformity with others (Kumar et al., 2019b). The patches of homogeneous surfaces in the bead included the surfaces on the clay mineral and iron-alginate complex. The maximum phosphate adsorption capacity determined from the Langmuir model for MtIA is 48.78 mg PO_4^{3-}-P/g of dry beads. Compared to other clay-metal ion-alginate crosslinked beads, our MtIA bead showed better adsorption capacity (Table 2). Among the reported beads, zirconium (Zr)-bentonite alginate beads exhibited the best adsorption capacity of 20.83 mg/g (Xi et al., 2021), and our beads had ~2.3 times higher capacity than that. The Langmuir constant k_l is 0.0079 L/mg.

The dimensionless parameter of the equilibrium or sorption intensity (R_L) in the Langmuir model (Eq. (10)) was calculated using the sorption constant K_l (0.0079 L/mg) and the initial concentrations of phosphate (C_0 = 10–2515 mg PO_4^{3-}-P/L) ranged from 0.0479 to 0.9268 for different initial phosphate concentrations (Table S1) and that suggests that the phosphate adsorption by MtIA is favorable (adsorption is unfavorable if $R_L > 1$, linear if $R_L = 1$, favorable if $0 < R_L < 1$ and irreversible if $R_L = 0$) (Weber and Chakravorti, 1974).

$$R_L = \frac{1}{1 + C_0\, K_l} \quad (10)$$

The experimental data did not fit the Sips and Temkin models well and were not considered for further evaluation.

3.5. Phosphate removal mechanism

From the adsorption kinetics and isotherm data, it is clear that phosphate adsorption onto the MtIA beads is governed by chemisorption and heterogeneity of the surface of the MtIA beads. There could be three possible adsorption sites in the MtIA beads which include: (1) iron present in the Fe-crosslinked in alginate, (2) entrapped montmorillonite clay mineral and (3) iron sorbed onto clay minerals. The phosphate removal mechanism is governed by ligand exchange, surface complexation, and electrostatic attraction. Both the clay mineral surface and amorphous iron oxide formed in the alginate network contain surface hydroxyl groups (−OH). Anionic phosphates ($H_2PO_4^-$/HPO_4^{2-}) are adsorbed onto the MtIA bead surface through ligand exchange between the –OH groups and phosphate ions (Xu et al., 2020). Phosphate ions also replace the surface –OH through ion-exchange. Further, iron ions can form iron oxide and hydroxide within the MtIA beads which can adsorb phosphate through inner-sphere surface complexation (Xi et al., 2021). While the SEM-EDS (Fig. 5a) data confirm the adsorption of phosphate by MtIA beads, the data could not pinpoint the possible active sites that adsorbed the phosphate.

FTIR data were collected from the fresh and spent MtIA beads to get information on molecular interaction in MtIA beads as they adsorbed phosphate (Fig. 5b). The characteristic P–O asymmetric bending should have appeared in the region ~1030 cm^{-1} (Jastrzebski et al., 2011) but it is not prominent enough. Therefore, the FTIR spectrum from the fresh MtIA beads was subtracted from that from the spent MtIA beads, and a peak is identified at ~995 cm^{-1} which confirms the complexation of phosphate with iron oxide (Ahmed et al., 2019; Karthikeyan et al., 2019).

Table 2
Phosphate adsorption performance of different clay-metal ion-alginate crosslinked beads.

Alginate Bead composition	Cross-linking ion	Solution pH	Concentration range (mg/L) tested	Dose (dry bead, g/L)	Adsorption capacity (PO_4^{3-}-P mg/g)	Source
Zr-alginate bentonite	Zr^{4+}	–	–	2	9.89	Kumar and Viswanathan (2017)
Ce-alginate bentonite	Ce^{3+}	–	–	2	8.52	Kumar and Viswanathan (2017)
La-alginate bentonite	La^{3+}	–	–	2	6.74	Kumar and Viswanathan (2017)
La-alginate-talc	La^{3+}	4	2.5–50	0.4	16.4	Wang et al. (2020)
Zr-alginate assisted kaolin	Zr^{4+}	–	0–45	2	12.12	Kumar and Viswanathan (2020)
Zr-bentonite alginate	Zr^{4+}	7	1.6–65	–	20.83	Xi et al. (2021)
Al-modified bentonite alginate	Ca^{2+}	3	1.6–13	2.6	5.14	Xu et al. (2020)
Al-pillared activated bentonite alginate	Ca^{2+}	5	2–27	2	6.23	Pawar et al. (2016)
MtIA beads	Fe^{3+}	6.5–7	0–2500	10.66	48.78	**This study**

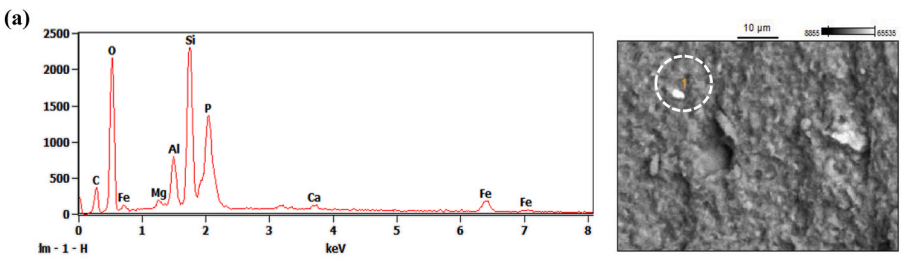

Element	C	O	Mg	Al	Si	P	Ca	Fe
Weight %	9.8±0.7	38.3±1.2	0.61±0.3	5.2±0.4	18.5±0.8	13.2±0.9	1.5±0.6	12.8±2.2

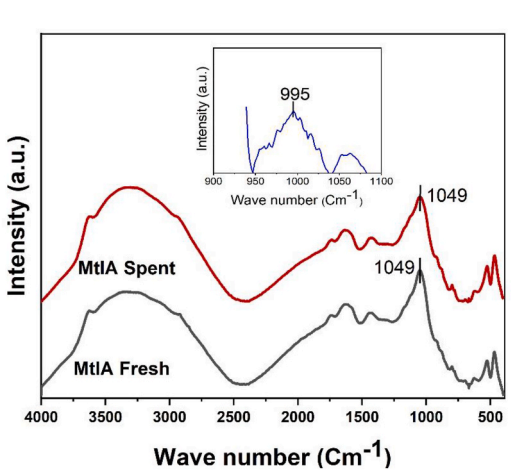

Fig. 5. (a) EDS spectra of spent MtIA beads (i.e., after phosphate adsorption); (b) FTIR spectra of MtIA beads before and after phosphate adsorption. Inset: Spectra at ~995 cm^{-1} in the spent beads confirmed the formation of iron-phosphate compounds (The spectrum obtained from the fresh MtIA beads was subtracted from that of the spent MtIA beads).

4. Conclusions

In this present work, the natural montmorillonite-incorporated iron crosslinked alginate (MtIA) beads designed for phosphate removal were fabricated using an easy to adopt sol-gel process. In this study, both clay mineral and iron participated in the phosphate removal process. While additional studies will be needed, the use of clay mineral is expected to help in making the beads sturdier. Material characterization data from FTIR and SEM-EDS have indicated that both clay particles and iron took part in the crosslinking with the alginate chain. The SEM micrographs of MtIA beads showed a heterogeneous rough-textured surface. The surface roughness of the MtIA beads facilitated the contact between phosphate ions and the beads, and thus improved the phosphate removal performance by the beads. The MtIA beads also effectively (~100%) removed low concertation phosphate (100 µg/L, eutrophic lake) within 30 min. The reaction kinetic data fitted into a pseudo-second-order model indicating that the adsorption mechanism was governed by chemisorption, and that was further confirmed by fitting the data into the Elovich model. The adsorption data fitted in the Freundlich isotherm model (R^2 = 0.9846), and model-derived parameters have indicated that adsorption sites in the MtIA beads are heterogeneous, and adsorption of phosphate onto the MtIA bead surface is a favorable process. The maximum adsorption capacity of the bead evaluated using the Langmuir model (R^2 = 0.9892) was found to be 48.78 mg PO_4^{3-}-P/g of dry beads which at least ~2.3 higher than other reported values for clay-metal-alginate beads. Phosphate removal was not affected by any change in pH (2-10). The beads are expected to find possible applications in phosphate removal from eutrophic lakes as well as municipal wastewater and agricultural runoff (specifically, tile drainage).

Declaration of competing interest

The authors declare that they have no known competing financial interests or personal relationships that could have appeared to influence the work reported in this paper.

Acknowledgments

This work was funded by National Science Foundation (NSF Grant# CBET-1707093), United States, USGS-North Dakota Water Resources Research Institute, United States, and North Dakota State University (NDSU Grand Challenges Initiative), United States. Tonoy Das received funding through NS-ICAR-IF from the Indian Council of Agricultural Research, India. Electron microscopy was done at the NDSU Core Laboratory (NSF Grant# CMMI-0821655).

Appendix B. Supplementary data

Supplementary data to this article can be found online at https://doi.org/10.1016/j.chemosphere.2021.130837.

CRediT author statement

Tonoy K. Das: Conceptualization, Methodology, Data curation, Formal analysis, Visualization, Writing – original draft, Investigation. Quentin Scott: Data curation, Visualization, Formal analysis. Achintya N. Bezbaruah: Supervision, Resources, Validation, Writing – review & editing, Project administration, Funding acquisition.

References

Ahmed, A.A., Gypser, S., Leinweber, P., Freese, D., Kuhn, O., 2019. Infrared spectroscopic characterization of phosphate binding at the goethite-water interface. Phys. Chem. Chem. Phys. 21, 4421–4434.

Almeelbi, T., Bezbaruah, A., 2012. Aqueous phosphate removal using nanoscale zero-valent iron. J. Nanoparticle Res. 14.

Bacelo, H., Pintor, A.M.A., Santos, S.C.R., Boaventura, R.A.R., Botelho, C.M.S., 2020. Performance and prospects of different adsorbents for phosphorus uptake and recovery from water. Chem. Eng. J. 381, 122566.

Barreca, S., Orecchio, S., Pace, A., 2014. The effect of montmorillonite clay in alginate gel beads for polychlorinated biphenyl adsorption: isothermal and kinetic studies. Appl. Clay Sci. 99, 220–228.

Bezbaruah, A.N., Krajangpan, S., Chisholm, B.J., Khan, E., Bermudez, J.J.E., 2009. Entrapment of iron nanoparticles in calcium alginate beads for groundwater remediation applications. J. Hazard Mater. 166, 1339–1343.

Bormans, M., Marsalek, B., Jancula, D., 2016. Controlling internal phosphorus loading in lakes by physical methods to reduce cyanobacterial blooms: a review. Aquat. Ecol. 50, 407–422.

Boyd, C.E., 2019. Phosphorus. Water Quality: an Introduction. Springer Nature.

Carpenter, S.R., 2005. Eutrophication of aquatic ecosystems: bistability and soil phosphorus. Proc. Natl. Acad. Sci. U. S. A 102, 10002–10005.

Dodds, W.K., Bouska, W.W., Eitzmann, J.L., Pilger, T.J., Pitts, K.L., Riley, A.J., Schloesser, J.T., Thornbrugh, D.J., 2009. Eutrophication of US freshwaters: analysis of potential economic damages. Environ. Sci. Technol. 43, 12–19.

Duan, H.T., Tao, M., Loiselle, S.A., Zhao, W., Cao, Z.G., Ma, R.H., Tang, X.X., 2017. MODIS observations of cyanobacterial risks in a eutrophic lake: implications for long-term safety evaluation in drinking-water source. Water Res. 122, 455–470.

Eaton, A., Clesceri, L.S., Rice, E.W., Greenberg, A.E., Franson, M., 2005. APHA: standard methods for the examination of water and wastewater, Centennial Edition. APHA, AWWA, WEF, Washington, DC.

Fabryanty, R., Valencia, C., Soetaredjo, F.E., Putro, J.N., Santoso, S.P., Kurniawan, A., Ju, Y.H., Ismadji, S., 2017. Removal of crystal violet dye by adsorption using bentonite - alginate composite. Journal of Environmental Chemical Engineering 5, 5677–5687.

Food and Agriculture Organization (FAO), 2020. FAOSTAT: Fertilizers Archive. http://www.fao.org/faostat/en/#data/RA.

Fernandes, R.D., de Moura, M.R., Glenn, G.M., Aouada, F.A., 2018. Thermal, microstructural, and spectroscopic analysis of Ca^{2+} alginate/clay nanocomposite hydrogel beads. J. Mol. Liq. 265, 327–336.

Fernandes, R.S., de Moura, M.R., Aouada, F.A., 2017. Optimization of synthesis of intercalated nanocomposite hidrogels for future application in the medical area. Quim. Nova 40, 60–67.

Gérard, F., 2016. Clay minerals, iron/aluminum oxides, and their contribution to phosphate sorption in soils—a myth revisited. Geoderma 262, 213–226.

Glibert, P.M., 2020. Harmful algae at the complex nexus of eutrophication and climate change. Harmful Algae 91.

Ho, Y.S., McKay, G., 1998. Kinetic models for the sorption of dye from aqueous solution by wood. Process Saf. Environ. Protect. 76, 183–191.

Hossain, M.E., Ritt, C.L., Almeelbi, T.B., Bezbaruah, A.N., 2018. Biopolymer beads for aqueous phosphate removal: possible applications in eutrophic lakes. Journal of Environmental Engginerring 144 (5), 04018030.

Jastrzebski, W., Sitarz, M., Rokita, M., Bulat, K., 2011. Infrared spectroscopy of different phosphates structures. Spectrochim. Acta Mol. Biomol. Spectrosc. 79, 722–727.

Jing, L.D., Liu, X.L., Bai, S., Wu, C.X., Ao, H.Y., Liu, J.T., 2015. Effects of sediment dredging on internal phosphorus: a comparative field study focused on iron and phosphorus forms in sediments. Ecol. Eng. 82, 267–271.

Karthikeyan, P., Banu, H.A.T., Meenakshi, S., 2019. Synthesis and characterization of metal loaded chitosan-alginate biopolymeric hybrid beads for the efficient removal of phosphate and nitrate ions from aqueous solution. Int. J. Biol. Macromol. 130, 407–418.

Kleinman, P.J.A., Sharpley, A.N., Withers, P.J.A., Bergstrom, L., Johnson, L.T., Doody, D. G., 2015. Implementing agricultural phosphorus science and management to combat eutrophication. Ambio 44, S297–S310.

Kumar, P.S., Korving, L., van Loosdrecht, M.C.M., Witkamp, G.J., 2019a. Adsorption as a technology to achieve ultra-low concentrations of phosphate: Research gaps and economic analysis. Water Res. X 4.

Kumar, V.K., Srinivas, G., Wood, B., Ramisetty, K.A., Stewart, A.A., Howard, C.A., Brett, D., Rodriquez-Reinoso, F., 2019b. Characterization of adsorption site energies and heterogeneous of porous materials. J. Mater. Chem. 7, 10104.

Kumar, I.A., Viswanathan, N., 2017. Fabrication of metal ions cross-linked alginate assisted biocomposite beads for selective phosphate removal. Journal of Environmental Chemical Engineering 5, 1438–1446.

Kumar, I.A., Viswanathan, N., 2020. Fabrication of zirconium(IV) cross-linked alginate/kaolin hybrid beads for nitrate and phosphate retention. Arabian Journal of Chemistry 13, 4111–4125.

Le Forestier, L., Muller, F., Villieras, F., Pelletier, M., 2010. Textural and hydration properties of a synthetic montmorillonite compared with a natural Na-exchanged clay analogue. Appl. Clay Sci. 48, 18–25.

Li, X.D., Zhang, Z.Y., Xie, Q., Yang, R.J., Guan, T., Wu, D.Y., 2019. Immobilization and release behavior of phosphorus on phoslock-inactivated sediment under conditions simulating the photic zone in eutrophic shallow lakes. Environ. Sci. Technol. 53, 12449–12457.

Lin, J., Qiu, P.H., Yan, X.J., Xiong, X., Jing, L.D., Wu, C.X., 2015. Effectiveness and mode of action of calcium nitrate and phoslock (R) in phosphorus control in contaminated sediment, a microcosm study. Water Air Soil Pollut. 226.

Liu, R.T., Chi, L.N., Wang, X.Z., Sui, Y.M., Wang, Y., Arandiyan, H., 2018. Review of metal (hydr)oxide and other adsorptive materials for phosphate removal from water. Journal of Environmental Chemical Engineering 6, 5269–5286.

Meinikmann, K., Hupfer, M., Lewandowski, J., 2015. Phosphorus in groundwater discharge - a potential source for lake eutrophication. J. Hydrol. 524, 214–226.

Michot, L.J., Bihannic, I., Porsch, K., Maddi, S., Baravian, C., Mougel, J., Levitz, P., 2004. Phase diagrams of Wyoming Na-montmorillonite clay. Influence of particle anisotropy. Langmuir 20 (25), 10829–10837.

Namduri, H., Nasrazadani, S., 2008. Quantitative analysis of iron oxides using Fourier transform infrared spectrophotometry. Corrosion Sci. 50, 2493–2497.

Ober, J.A., 2016. Mineral Commodity Summaries 2016. US Geological Survey.

Papageorgiou, S.K., Kouvelos, E.P., Favvas, E.P., Sapalidis, A.A., Romanos, G.E., Katsaros, F.K., 2010. Metal-carboxylate interactions in metal-alginate complexes studied with FTIR spectroscopy. Carbohydr. Res. 345, 469–473.

Patle, T., Khaddar, V., Tiwari, R., Para, P., 2019. Evaluation of phosphorus availability and phosphorus fixation in four different soils orders. J. Pharmacogn. Phytochem. 8, 2087–2090.

Pawar, R.R., Gupta, P., Lalhmunsiama Bajaj, H.C., Lee, S.M., 2016. Al-intercalated acid activated bentonite beads for the removal of aqueous phosphate. Sci. Total Environ. 572, 1222–1230.

Ramasahayam, S.K., Guzman, L., Gunawan, G., Viswanathan, T., 2014. A comprehensive review of phosphorus removal technologies and processes. J. Macromol. Sci., Pure Appl. Chem. 51, 538–545.

Randall, M.C., Carling, G.T., Dastrup, D.B., Miller, T., Nelson, S.T., Rey, K.A., Hansen, N. C., Bickmore, B.R., Aanderud, Z.T., 2019. Sediment potentially controls in-lake phosphorus cycling and harmful cyanobacteria in shallow, eutrophic Utah Lake. PloS One 14.

Ravi Pandey, L.M., 2019. Enhanced adsorption capacity of designed bentonite and alginate beads for the effective removal of methylene blue. Appl. Clay Sci. 169, 102–111.

Ritt, C.L., Chisholm, B.J., Bezbaruah, A.N., 2019. Assessment of molecularly imprinted polymers as phosphate sorbents. Chemosphere 226, 395–404.

Robertson, D.M., Rose, W.J., Saad, D.A., 2003. Water Quality and the Effects of Changes in Phosphorus Loading to Muskellunge Lake, Vilas County, Wisconsin. US Department of the Interior, US Geological Survey.

Ruuhijarvi, J., Rask, M., Vesala, S., Westermark, A., Olin, M., Keskitalo, J., Lehtovaara, A., 2010. Recovery of the fish community and changes in the lower trophic levels in a eutrophic lake after a winter kill of fish. Hydrobiologia 646, 145–158.

Teng, H., Hsieh, C.T., 1999. Activation energy for oxygen chemisorption oil carbon at low temperatures. Ind. Eng. Chem. Res. 38, 292–297.

US Environmental Protection Agency (USEPA), 2009. Nutrient Control Design Manual: State of Technology Review Report.

Valderrama, C., Gamisans, X., de las Heras, X., Farran, A., Cortina, J.L., 2008. Sorption kinetics of polycyclic aromatic hydrocarbons removal using granular activated carbon: intraparticle diffusion coefficients. J. Hazard Mater. 157, 386–396.

Wang, C.H., Jiang, H.L., 2016. Chemicals used for in situ immobilization to reduce the internal phosphorus loading from lake sediments for eutrophication control. Crit. Rev. Environ. Sci. Technol. 46, 947–997.

Wang, B., Zhang, W., Li, L., Guo, W.B., Xing, J., Wang, H.Y., Hu, X.L., Lyu, W.L., Chen, R. F., Song, J.Y., Chen, L., Hong, Z.Z., 2020. Novel talc encapsulated lanthanum alginate hydrogel for efficient phosphate adsorption and fixation. Chemosphere 256.

Weber, T.W., Chakravorti, R.K., 1974. Pore and solid diffusion models for fixed-bed adsorbers. AIChE J. 20, 228–238.

Weber, W.J., Morris, J.C., 1963. Kinetics of adsorption on carbon from solution. J. Sanit. Eng. Div. 89, 31–60.

Wetzel, R.G., 2001. Limnology: Lake and River Ecosystems. Gulf Professional Publishing.

Xi, H., Li, Q.Q., Yang, Y., Zhang, J.F., Guo, F., Wang, X.G., Xu, S.K., Ruan, S.P., 2021. Highly effective removal of phosphate from complex water environment with porous Zr-bentonite alginate hydrogel beads: Facile synthesis and adsorption behavior study. Appl. Clay Sci. 201.

Xu, X.Y., Wang, B., Tang, H., Jin, Z.X., Mao, Y.L., Huang, T.Y., 2020. Removal of phosphate from wastewater by modified bentonite entrapped in Ca-alginate beads. J. Environ. Manag. 260.

Yang, Y., Shi, X., Ballent, W., Mayer, B.K., 2017. Biological phosphorus recovery: review of current progress and future needs. Water Environ. Res. 89, 2122–2135.

Zhang, H.Y., Shi, Y.S., Xu, X.F., Zhang, M., Ma, L., 2020. Structure regulation of bentonite-alginate nanocomposites for controlled release of imidacloprid. ACS Omega 5, 10068–10076.